Available online at www.sciencedirect.com
SCIENCE DIRECT
Journal of Power Sources 157 (2006) 325–334
JOURNAL OF POWER SOURCES
www.elsevier.com/locate/jpowsour

Two-dimensional transient model of a cascaded micro-tubular solid oxide fuel cell fed with methane

Pedro Nehter *

Fuel Cells Laboratory, Faculty of Mechanical Engineering, Hamburg University of Applied Sciences, Berliner Tor 21, D-20099 Hamburg, Germany

Received 21 April 2005; received in revised form 8 July 2005; accepted 22 July 2005
Available online 17 October 2005

Abstract

A two-dimensional transient simulation model for a cascaded (10 cascades) micro-tubular solid oxide fuel cell (SOFC) and a common micro-tubular SOFC with a preheater tub was developed to calculate the distribution of gas species, the local current, voltage and temperature. The goal was to compare these two different SOFC designs under steady state and load change conditions with respect to power density. Steady state simulation results have shown that the cascaded cell concept is able to operate at higher average cell voltages in principle. Compared to the cascaded cell concept the average ohmic anodic and cathodic resistance of the common cell has to be 84 times lower to reach the same average power density at an average voltage of 0.7 V. The cascaded cell concept gives the opportunity to operate at a higher average voltage than the lowest Nernst voltage offers. This could be interesting to realize high fuel utilization (>85%). Transient simulation results have shown that both cell concepts respond within 10 s on an electrical load change. The cascaded cell concept has shown a lower temporary voltage drop than the common cell concept. This paper describes the theory, solution techniques and results.

Keywords: SOFC; Transient; Cascaded; Micro-tubular; Thermodynamic analysis

1. Introduction

The micro-tubular SOFC has advantages due to rapid start-up [1], load change behavior and the volume related power density [2] because the cell area per volume increases by decreasing the cell diameter. The thermal integration of heat sinks is an important issue to simplify SOFC systems. The large scaled tubular SOFC developed by Westinghouse consists of an air preheater tube to preheat the air directly by the generated heat. This concept gives the further opportunity to implement heat sinks like a stack-integrated prereformer. Thereby, the excess air demand is reduced. Thermodynamic and economic analyses have shown that the low excess air demand and stack-integrated heat sinks are a prerequisite to design low costs and efficiently SOFC systems [3]. Therefore, the air preheater tube is adopted for this investigation of micro-tubular SOFCs (Fig. 1).

The tubular SOFC of Siemens–Westinghouse has compared to the planar SOFC the disadvantage that the ohmic losses are much higher due to the longer ways of electrical current. The micro-tubular concept developed by Adelan Ltd., UK, uses wires to collect the current. This reduces the internal ways of electrical current in comparison to the tubular concept of Westinghouse. The planar concept provides the largest area for the current collector but it shows disadvantages in start-up time and mechanical stability. However, the ohmic resistance of a current collector is an important issue, which could have a strong influence on power density.

The local cell voltage is, from a thermodynamic point of view, limited by the local Nernst voltage. This means that the maximum voltage of common single cells with equipotential electrodes could reach the lowest Nernst voltage (highest fuel utilization). Cascaded concepts (Fig. 2) give the opportunity of realizing different voltages at the cascades. These voltages are added up to the all over cell voltage. If the cascaded average cell voltage has the same value as the single cell voltage, the entropy production must also have the same value as well.

Cascaded concepts have the advantage of reaching higher average voltages than the lowest Nernst voltage in the gas bulk. On the other hand current efforts are focussing on average voltages which where lower than the lowest Nernst voltages at a fuel

* Tel.: +49 40 42875 8789; fax: +49 40 42875 8783.
E-mail address: nehter@aol.com.

0378-7753/$ – see front matter © 2005 Elsevier B.V. All rights reserved.
doi:10.1016/j.jpowsour.2005.07.077

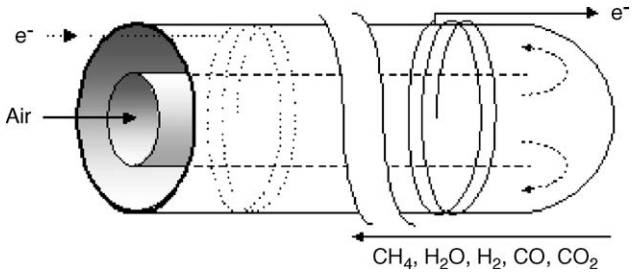

Fig. 1. Micro-tubular SOFC.

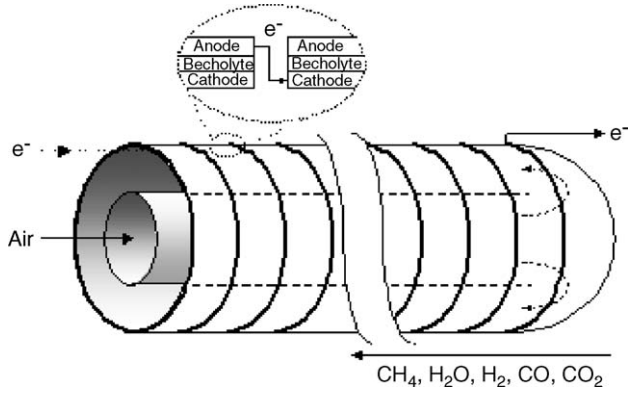

Fig. 2. Cascaded micro-tubular SOFC.

utilization of 85%. This leads to higher average power densities. In case of an increasing fuel utilization the cascaded concepts could be an interesting solution to reach layout voltages which where higher than the lowest Nernst voltage. Compared to common single cells, cascaded concepts are reducing the all over electrical current by the number of cascades. This could lead to lower ohmic polarization losses than the common single cell concept.

2. Model

2.1. Energy balance

For the determination of the cell's electrical performance it is necessary to know the cell's temperature distribution because the loss mechanisms are strongly temperature sensitive. Hall and Hall and Colclaser [4] proposed a one-dimensional transient model of a tubular SOFC, which uses Eq. (1) to calculate the temperature distribution of the solid ceramic of the SOFC. Heat transfer (Fig. 3) occurs through thermal conductivity, convection (q_α) and radiation (q_{rad}). The conductive heat transfer in the solid material of the cell can be calculated by solving the local energy balance.

$$\frac{\partial T}{\partial \tau} = a \,\text{div grad}\, T + \frac{\dot{q}}{\rho c_{\text{p}}} \tag{1}$$

Here T is the temperature, τ the time, ρ the solid mass density, c_{p} the specific heat, a the thermal conductivity coefficient of the solid ceramic of the SOFC and $\dot{q}$ is the volume specific heat source. It is assumed that the thermal conductivity coefficient is

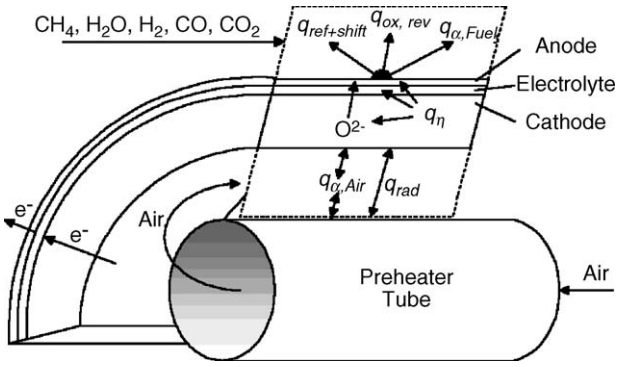

Fig. 3. Schematics of heat transfer.

constant and equal in each direction.

$$\text{div grad}\, T = \frac{1}{r}\frac{\partial T}{\partial r} + \frac{\partial^2 T}{\partial r^2} + \frac{\partial^2 T}{\partial z^2} \tag{2}$$

The differential equation is applied in axial and radial direction of the cell. The temperature profile in the circumferential direction is assumed to be homogenous.

There are heat sources due to the reaction enthalpy of the reforming, the shift reaction ($q_{\text{ref+shift}}$) and the reversible heat ($q_{\text{ox,rev}}$) of fuel oxidation, respectively.

$$\dot{q}_{\text{reac}} = \frac{1}{\Delta r\, \Delta A}(\Delta \dot{H}_{\text{ref}} + \Delta \dot{H}_{\text{shift}} + \Delta \dot{Q}_{\text{ox,rev}}) \tag{3}$$

This heat is equal to the difference of the all over reaction enthalpy and the reversible work of fuel oxidation.

$$\dot{q}_{\text{reac}} = \frac{1}{\Delta r\, \Delta A}(\Delta \dot{H}_{\text{reac}(T=\text{const})} - \dot{W}_{\text{ox,rev}}) \tag{4}$$

The oxidation of hydrogen and carbon monoxide are assumed to be the only electrochemical reactions. It can be shown that the reversible work of these two reactions have the same value if the shift reaction is fulfilling the equilibrium condition. Investigations of the reforming reaction of methane at Ni-cermet anodes [10] have shown that the shift reaction is near to equilibrium condition. The different mechanism losses of the hydrogen and carbon monoxide oxidation were neglected to determine the reversible work from only one of these reactions. The following Eq. (5) uses the reversible work of the hydrogen oxidation

$$\dot{q}_{\text{reac}} = \frac{1}{\Delta r\, \Delta A}\left[\sum_i \dot{n}_{i,\text{out}}\left(\Delta^b H_i^0 + \int_{T_0}^{T_{\text{S}}} c_{\text{p},i}(T)\,\text{d}T\right) - \sum_i \dot{n}_{i,\text{in}}\left(\Delta^b H_i^0 + \int_{T_0}^{T_{\text{S}}} c_{\text{p},i}(T)\,\text{d}T\right) - \dot{n}_{\text{H}_2,\text{ox}}\dot{W}_{\text{ox,rev}}\right] \tag{5}$$

which can be determined by the free reaction enthalpy of the hydrogen oxidation.

$$W_{\mathrm{ox,rev}} = \int_{\mathrm{uf},1}^{\mathrm{uf},2} \left(\Delta^r G_{(T)} + TR \ln \frac{p_{\mathrm{H_2O}}(\mathrm{uf})}{p_{\mathrm{H_2}}(\mathrm{uf})\sqrt{p_{\mathrm{O_2}}(\mathrm{uf})}} \right) \mathrm{d\,uf} \tag{6}$$

Convection occurs between solid surfaces and the gas streams.

$$\dot{q}_\alpha = \frac{\alpha(\mathrm{Nu})}{\Delta r}(\vartheta_{\mathrm{solid}} - \vartheta_{\mathrm{fluid}}) = \frac{1}{\Delta r\, \Delta A} \Delta \dot{H}_{\mathrm{fluid}} \tag{7}$$

where Δr the radial segment and ΔA the area segment perpendicular to flow direction of fuel and air.

It is assumed that radiation transfers only occur between the cathode and air preheater tube.

$$\dot{q}_{\mathrm{rad}} = \frac{C_{\mathrm{Ca,ft}}}{\Delta r} \left[\left(\frac{T_{\mathrm{Ca}}}{100} \right)^4 - \left(\frac{T_{\mathrm{ft}}}{100} \right)^4 \right] \tag{8}$$

Here is C the radiation exchange factor between cathode and the preheater tube.

The heat sources due to the polarization effects ($\dot{q}_\eta$) are expressed by

$$\dot{q}_\eta = \frac{\hat{\eta} i\, \Delta A_i}{\Delta r\, \Delta A} = \frac{R(i\, \Delta A_i)^2}{\Delta r\, \Delta A} = \frac{\delta R_\delta i^2\, \Delta A_i}{\Delta r\, \Delta A} \tag{9}$$

where $\hat{\eta}$ is the overpotential, i the current density, ΔA_i the area segment in the equivalent electrical current flow direction, R the equivalent ohmic resistance in Ω, R_δ the equivalent specific ohmic resistance in $\Omega\,\mathrm{m}$ and δ is the thickness of equivalent ohmic resistance.

2.2. Mass balance

For the calculation the fluid channel is divided into slices in the same distances as assumed for the cell. For the simplification the gas composition is assumed to be homogenous distributed in each gas slice. The chemical species CH_4, H_2, H_2O, CO, CO_2 for fuel and O_2, N_2 for oxidant are considered in this study. It is assumed that all the gases are ideal and incompressible fluids. The considered chemical reactions are:

$\mathrm{CH_4 + H_2O \leftrightarrow 3H_2 + CO}$ Steam reforming

$\mathrm{CO + H_2O \leftrightarrow CO_2 + H_2}$ Shift reaction

$\mathrm{H_2 + 0.5O_2 \leftrightarrow H_2O}$ Hydrogen oxidation

In this study, the oxidation of carbon monoxide is neglected. The reversible work of the hydrogen oxidation and carbon monoxide oxidation have the same value if the shift reaction fulfills the equilibrium condition

$$\frac{x_{\mathrm{H_2}}\, x_{\mathrm{CO_2}}}{x_{\mathrm{CO}}\, x_{\mathrm{H_2O}}} = \exp\left(-\frac{\Delta_r H - T\, \Delta_r S}{RT} \right) \tag{10}$$

where x is the molar fraction of reacting species, $\Delta_r H$ is the reaction enthalpy and $\Delta_r S$ is the reaction entropy. The investigations of the shift reaction at Ni-cermet anodes have shown [10,11] that the conversion rates are always near to equilibrium condition.

The reforming reaction is a kinetic controlled reaction. Some investigations [9] at Ni-cermet anodes shown that boundary diffusion and pore diffusion can be neglected below 700 °C and boundary diffusion can be neglected between 800 and 900 °C [12]. In this study, both transport processes were neglected. The conversion of methane is given [10] as

$$\dot{n}_{\mathrm{CH_4},0} - \dot{n}_{\mathrm{CH_4}} = \Delta A_{\mathrm{Kat}}\, k_{\mathrm{eff}}\, p_{\mathrm{CH_4}}\, p_{\mathrm{H_2O}} \tag{11}$$

where ΔA_{Kat} is the catalytic area calculated by the geometry of the anode, k_{eff} the effective rate coefficient and p the partial pressure of gas species. The conversion rate coefficient is determined by the Arrhenius equation

$$k_{\mathrm{eff}} = k_0 \exp\left(-\frac{E_{\mathrm{Act}}}{RT} \right) \tag{12}$$

where k_0 is the pre-exponential coefficient and E_{Act} the activation energy. The boundary of conversion rate is given by the thermodynamic equilibrium:

$$\frac{x_{\mathrm{H_2}}^3\, x_{\mathrm{CO}}}{x_{\mathrm{CH_4}}\, x_{\mathrm{H_2O}}} = \left(\frac{p^0}{p} \right)^2 \exp\left(-\frac{\Delta_r H - T\, \Delta_r S}{RT} \right) \tag{13}$$

The local conversion of the hydrogen oxidation is determined by Faradays law as follows:

$$\dot{n}_{\mathrm{H_2},0} - \dot{n}_{\mathrm{H_2}} = \frac{i\, \Delta A}{2F} \tag{14}$$

$$\dot{n}_{\mathrm{O_2},0} - \dot{n}_{\mathrm{O_2}} = \frac{i\, \Delta A}{4F} \tag{15}$$

The all over fuel utilization, uf, can be calculated by the cell current I, number of cascades n_{cas} and inlet gas composition

$$\mathrm{uf} = \frac{I\, n_{\mathrm{cas}}}{F(8\dot{n}_{\mathrm{CH_4},0} + 2\dot{n}_{\mathrm{CO},0} + 2\dot{n}_{\mathrm{H_2},0})} \tag{16}$$

In case of steady state calculations the inlet mass flow is determined iteratively to reach a requested fuel utilization.

2.3. Electrochemical approaches

Polarization is a common parameter in the analysis of fuel cell performance. To calculate the relationship between local voltage $U_{\mathrm{Cell},L}$ and local current density the following general expression can be used:

$$U_{\mathrm{Cell},L} = \bar{U}_{\mathrm{Nernst}} - \hat{\eta}_{\mathrm{Act,An}} - \hat{\eta}_{\mathrm{Act,Ca}} - \hat{\eta}_{\mathrm{Diff,An}} - \hat{\eta}_{\mathrm{Diff,Ca}} - \hat{\eta}_{\Omega,\mathrm{Elt}} \tag{17}$$

The overpotential can be divided in activation, diffusion (concentration) and ohmic overpotential. The Nernst voltage is considered to be the driving force, which is a function of the

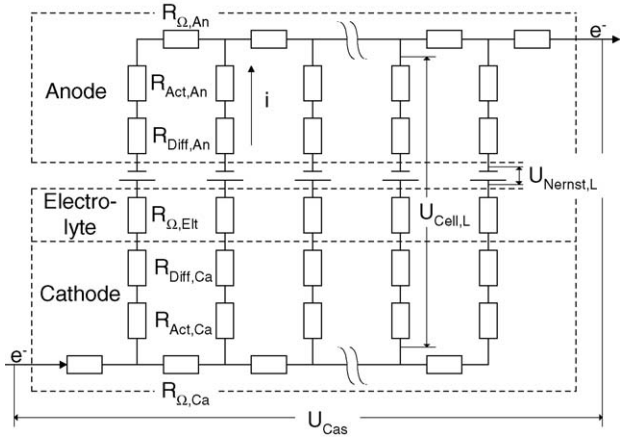

Fig. 4. Equivalent electrical circuit.

reversible work of the hydrogen oxidation (Eq. (6)).

$$\bar{U}_{\text{Nernst}} = -\frac{W_{\text{ox,rev}}}{\Delta\text{uf}\,2F} \tag{18}$$

For calculating the resulting voltage of one cascade further ohmic resistances ($R_{\Omega,\text{An}}$, $R_{\Omega,\text{Ca}}$ as shown in Fig. 4) have to be taken into account. The voltage drop over these ohmic resistances is determined iteratively by using Kirchhoff's law and the local voltages $U_{\text{Cell},L}$.

2.4. Activation overpotential

The activation of a chemical reaction involves energy barriers, which must be overcome by the reacting species. These energy barriers are called the activation energy and result in activation or charge transfer polarization. The activation polarization of an electrochemical reaction is usually expressed by the well-known Butler–Volmer equation

$$i = i_0 \left[\exp\left(\frac{\hat{\alpha} z F \hat{\eta}_{\text{Act}}}{RT}\right) - \exp\left(-\frac{(1-\hat{\alpha}) z F \hat{\eta}_{\text{Act}}}{RT}\right)\right] \tag{19}$$

where $\hat{\alpha}$ is the transfer coefficient and i_0 the exchange current density. The transfer coefficient, which is approximately 0.5 for fuel cells, is considered to be the fraction of the change in polarization that leads to a change in the reaction rate constant and its value. The exchange current density is the cathodic and anodic electrode reaction rate at the equilibrium potential. A high exchange current density means that good fuel cell performance can be expected. With $\hat{\alpha} = 0.5$ (Eq. (19)) the activation polarization can be calculated as follows:

$$\hat{\eta}_{\text{Act}} = \frac{RT}{0.5 z F} \exp\left(\frac{i}{2 i_0}\right) \tag{20}$$

For the anodic exchange current density of the hydrogen oxidation at Ni–YSZ anodes, Mogensen and Lindegaard [5] has proposed Eq. (21).

$$i_{0,\text{An}} = \gamma_{\text{An}} \left(\frac{p_{\text{H}_2}}{p_{0,\text{An}}}\right) \left(\frac{p_{\text{H}_2\text{O}}}{p_{0,\text{An}}}\right) \exp\left(-\frac{E_{\text{Act,An}}}{RT}\right) \tag{21}$$

where $E_{\text{Act,An}}$ is the activation energy, γ_{An} an empirical pre-exponential factor, p_{H_2} the partial pressure of hydrogen, $p_{\text{H}_2\text{O}}$ the partial pressure of water and $p_{0,\text{An}}$ is the reference pressure at the anode.

The cathodic exchange current density of LSM cathodes is expressed as [13]:

$$i_{0,\text{Ca}} = \gamma_{\text{Ca}} \left(\frac{p_{\text{O}_2}}{p_{0,\text{Ka}}}\right)^{0.25} \exp\left(-\frac{E_{\text{Act,Ca}}}{RT}\right) \tag{22}$$

2.4.1. Concentration overpotential

The concentration overpotential is a fictive electrical potential drop caused by the concentration difference in the gas phase. Diffusion through the porous material is typically described by binary molecular diffusion and Knudsen diffusion. In this study both types of diffusion are taken into account to estimate the concentration overpotential. It is assumed that the concentration gradient along the pore is much higher than the concentration gradient inside the surface boundary. Only the concentration gradient in the porous electrodes is taken into account.

For the ideal gas model the anodic concentration overpotential, which is proportional to the irreversible entropy production can be written as

$$\hat{\eta}_{\text{Diff,An}} = \frac{RT}{zF} \ln\left(\frac{p^*_{\text{H}_2}}{p^0_{\text{H}_2}} \frac{p^0_{\text{H}_2\text{O}}}{p^*_{\text{H}_2\text{O}}}\right) = \frac{T}{zF} \Delta S_{\text{irr,An}} \tag{23}$$

and for the cathodic concentration overpotential as follows:

$$\hat{\eta}_{\text{Diff,Ca}} = \frac{RT}{2zF} \ln\left(\frac{p^*_{\text{O}_2}}{p^0_{\text{O}_2}}\right) = \frac{T}{2zF} \Delta S_{\text{irr,Ca}} \tag{24}$$

where p^0 is the partial pressure in the gas bulk, p^* the partial pressure at the end of the pores. The concentration profiles inside the pores can be estimated by using the Fick's law (Eqs. (25)–(27)). The molar fraction x can be expressed as

$$x^*_{\text{H}_2} = x^0_{\text{H}_2} - \frac{RTi\delta_{\text{An}}}{p2FD_{\text{eff,An}}} \tag{25}$$

$$x^*_{\text{H}_2\text{O}} = x^0_{\text{H}_2\text{O}} + \frac{RTi\delta_{\text{An}}}{p2FD_{\text{eff,An}}} \tag{26}$$

for the equimolar diffusion of hydrogen and water and

$$x^*_{\text{O}_2} = 1 + (x^0_{\text{O}_2} - 1) \exp\left(\frac{RTi\delta_{\text{Ca}}}{p4FD_{\text{eff,Ca}}}\right) \tag{27}$$

for the self-diffusion of oxygen in nitrogen. δ_{An} is the thickness of the anode, δ_{Ca} the thickness of the cathode and D_{eff} the effective diffusion coefficient. In this model, the effective diffusion coefficient takes the Knudsen diffusion as well as the ordinary diffusion at the cathode and the binary diffusion at the anode into account.

The binary diffusion coefficient between gas species A and B in free space is given by the Chapman–Enskog theory

$$D_{AB} = 1.8583 \times 10^{-6} \left(\frac{1}{M_A} + \frac{1}{M_B}\right)^{1/2} \frac{T^{3/2}}{p\sigma^2_{AB}\Omega_D} \tag{28}$$

where σ is the collision diameter (Lennard–Jones length) and Ω_D is the collision integral based on the Lennard–Jones potential. Neufield et al. [6] has proposed the following approach

$$\Omega_D = \frac{1.06036}{(kT/\varepsilon_{AB})^{0.15610}} + \frac{0.19300}{\exp(0.47635(kT/\varepsilon_{AB}))} + \frac{1.03587}{\exp(1.52996(kT/\varepsilon_{AB}))} + \frac{1.76474}{\exp(3.89411(kT/\varepsilon_{AB}))} \quad (29)$$

to calculate the collision integral by the Lennard–Jones energy ε, which is a function of the critical gas properties and Boltzmann constant k.

The Knudsen diffusion coefficient for a species A is defined as

$$D_{\mathrm{Kn},A} = \frac{2R_{\mathrm{Por}}\bar{v}_A}{3} \quad (30)$$

where R_{Por} is the pore radius and $\bar{v}$ is the average velocity of the gas molecule. Both ordinary diffusion and Knudsen diffusion can be combined within the effective diffusion coefficient which can be written as:

$$\frac{1}{D_{\mathrm{eff,Por},A}} = \frac{\tau_\mathrm{p}}{\theta}\left(\frac{1}{D_{AB}} + \frac{1}{D_{\mathrm{Kn},A}}\right) \quad (31)$$

The tortuosity τ_p and porosity θ are used to account the geometry of the pores and relation between solid space and pore space of the electrode.

If we neglect the presence of other species except hydrogen and water inside the anodic pores, the anodic effective diffusion coefficient can be expressed for the ideal gas mixture as [7]:

$$D_{\mathrm{eff,An}} = \left(\frac{p_{\mathrm{H_2O}}}{p_{\mathrm{ges}}}\right) D_{\mathrm{eff,Por,H_2}} + \left(\frac{p_{\mathrm{H_2}}}{p_{\mathrm{ges}}}\right) D_{\mathrm{eff,Por,H_2O}} \quad (32)$$

Inside the cathodic pores the cathodic effective diffusion coefficient can be formulated as

$$D_{\mathrm{eff,Ca}} = D_{\mathrm{eff,Por,O_2}} \quad (33)$$

2.4.2. Ohmic overpotential

Ohmic losses occur according to the flow of ions in the electrolyte

$$\hat{\eta}_{\Omega,\mathrm{Elt}} = iR_{\Omega,\mathrm{Elt}} \quad (34)$$

and the flow of electrons through the electrode materials.

$$\hat{\eta}_{\Omega,\mathrm{An}} = iR_{\Omega,\mathrm{An}} \quad (35)$$

$$\hat{\eta}_{\Omega,\mathrm{Ca}} = iR_{\Omega,\mathrm{Ca}} \quad (36)$$

The ionic conductivity of the electrolyte depends strongly on material, temperature T and thickness δ. For YSZ electrolytes Achenbach et al. [8] has proposed the following dependency:

$$R_{\Omega,\mathrm{Elt}} = \delta_{\mathrm{Elt}} \frac{1\,\Omega\,\mathrm{m}}{33,400\,\exp(-10,300K/T)} \quad (37)$$

In this study, the electronic resistances of the anode and cathode are assumed as constant.

2.5. Solution technique

The model includes the calculation of chemical reactions like the steam reforming, shift reaction, electrochemical reactions and thermal heat transfer. The thermal part of the model accepts the cell electrical output and the cell heat sources from the electrochemical part and calculates new cell temperature. Overpotential and Kirchhoff's law are used to determine the local current density and local cell voltage. The local cell currents are summed up to the total cell current. The cell voltage is determined by the sum of cascade voltages. For the calculation of steady state conditions the calculated cell voltage is compared with the requested cell voltage. Cell heat sources are calculated from reversible entropy change due to the oxidation of hydrogen, the local overpotential, the heat transfer by radiation and the heat transfer by convection, which includes the sensible enthalpy changes in the gaseous phases. These heat sources are applied to the solid nodes of the thermal SOFC model to calculate the new cell temperature by solving Eq. (1). The transient model uses the Cranck–Nicolson discretization (axial: 51 nodes; radial: 7 nodes), which has the advantage that no stability boundaries have to be considered. The generated 2D-tridiagonal matrix is solved iteratively by the Gauss–Seidel method. Fig. 5 shows a flow chart of this process. This model can also calculate steady state operation points by running transient simulations until the transient decay to a level below a specified amount.

The model is used to determine the transient response as a consequence of the electrical load changes. The cell is subjected to a step of increasing current and a time dependent increment of input molar gas flows

$$\dot{n}(\tau) = \dot{n}(\tau = 0) + [\dot{n}(\tau = \infty) - \dot{n}(\tau = 0)](1 - \exp(-\tau/\tau_C)) \quad (38)$$

where τ is the time after the load change and τ_C is the time constant. Hereby the input gas compositions are held constant.

3. Results

The current and temperature distributions at the steady state and transient conditions are simulated for both the common single micro-tubular cell and the cascaded micro-tubular cell. The initial parameters are listed in Table 1. In this study, temperatures of the fuel and the oxidant at the inlets of the cell are assumed to be the same.

3.1. Steady state characteristic

The temperature distribution of the common micro-tubular cell is shown in Fig. 6. In comparison to the results of large scaled tubular SOFC reported by Siemens–Westinghouse [14] the qualitatively temperature profile of the micro-tubular SOFC shows similar tendency. However, the deviation between experimental data and simulation data indicates that the future comparison to measured data of micro-tubular SOFC is necessary.

The molar fraction profile along the flow direction (z-direction from fuel inlet) is shown in Fig. 7.

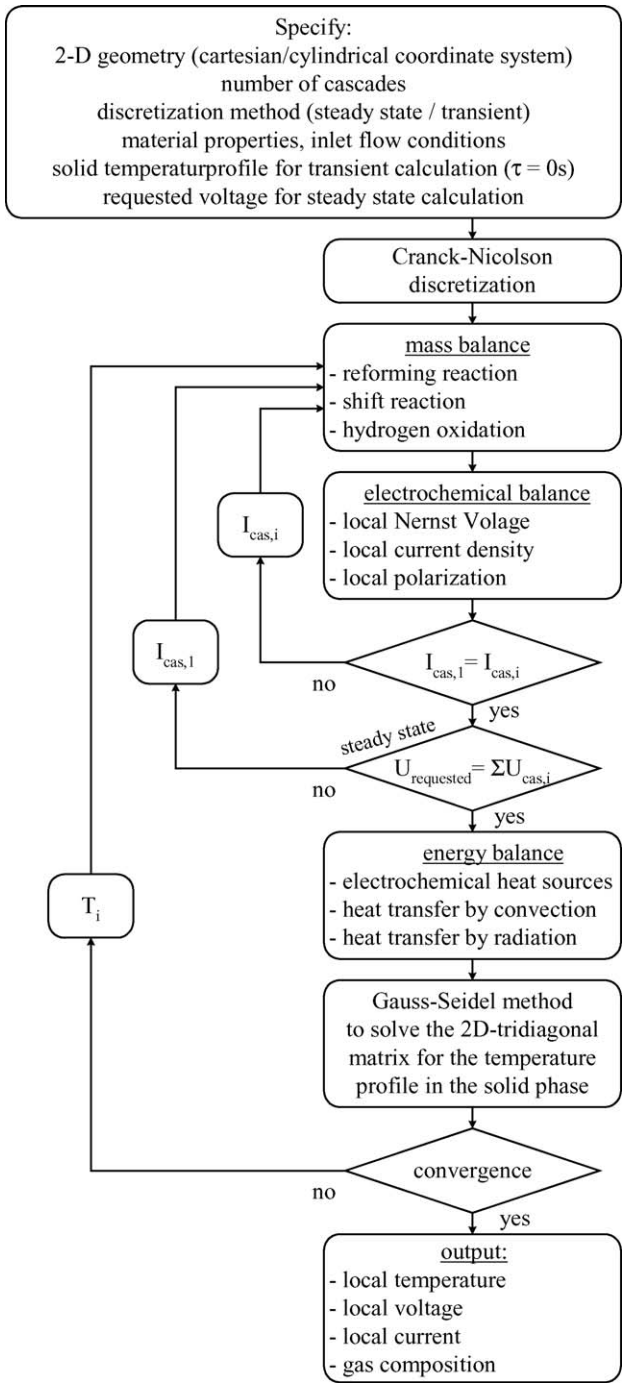

Fig. 5. Flowchart of solution technique.

In the first section of the fuel cell, the hydrogen fraction increases due to the endothermic reforming of methane. This has the effect of cell cooling at the fuel inlet. The decreasing of hydrogen fraction occurs by the electrochemical oxidation of hydrogen, which is proportional to the local current density (Fig. 8). Thereupon, the shift reaction produces hydrogen as long as carbon monoxide is available.

As shown in Fig. 8, the local Nernst voltage decreases due to this drop of hydrogen and carbon monoxide. In the common micro-tubular cell, the local current density increases along the

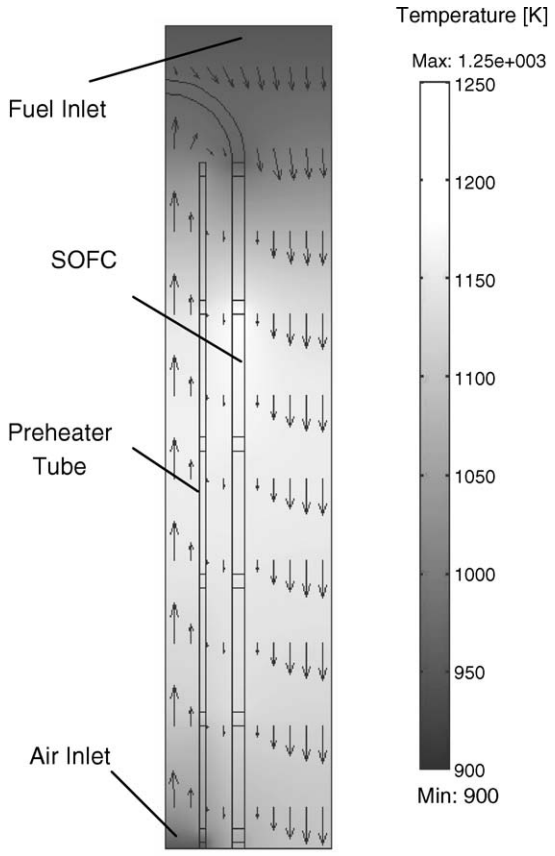

Fig. 6. Temperature profile of the common micro-tubular cell.

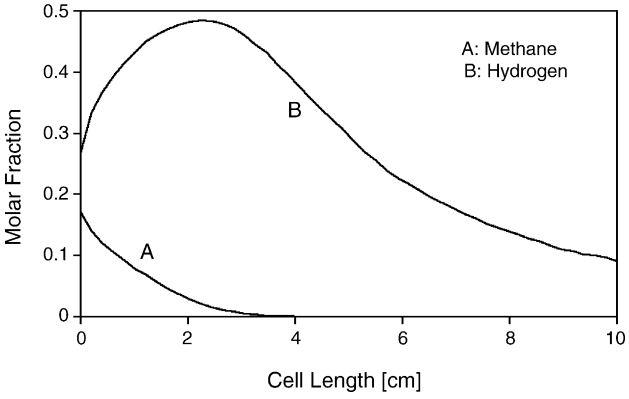

Fig. 7. Hydrogen and methane fraction of the common cell.

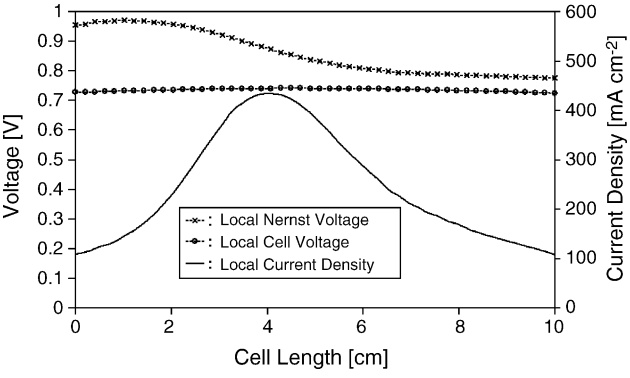

Fig. 8. Local voltage and current density of the common cell.

Table 1
Initial parameters

Number of cascades	10
Cell length [m]	0.1
Cell inside diameter [m]	2×10^{-3}
Thickness anode (Ni–YSZ) [m]	0.05×10^{-3}
Thickness cathode ($La_{0.6}Sr_{0.4}MnO_3$) [m]	0.05×10^{-3}
Thickness electrolyte (YSZ) [m]	0.1×10^{-3}
Heat capacity ceramic [J kg^{-1} K^{-1}]	400
Heat conduction coefficient ceramic [W m^{-1} K^{-1}]	2
Density ceramic [kg m^{-3}]	6600
Air preheater tube diameter [m]	1×10^{-3}
Thickness air preheater tube [m]	0.1×10^{-3}
Heat conduction coefficient air preheater tube [W m^{-1} K^{-1}]	6
Pre-exponential coefficient for exchange current density anode [A m^{-2}]	18.9×10^9
Pre-exponential coefficient for exchange current density cathode [A m^{-2}]	1034×10^9
Activation energy anode [kJ mol^{-1}]	120
Activation energy cathode [kJ mol^{-1}]	130
Activation energy reference [kJ mol^{-1}]	150
Ohmic resistance anode cascaded [Ω m]	5.6×10^{-6}
Ohmic restistance cathode cascaded [Ω m]	5.6×10^{-6}
Radiation exchange factor [W m^{-2} K^{-4}]	0.1059
Temperature gas inlet [K]	973.15
Pressure gas inlet [bar]	1.04
Fuel inlet flow [mol s^{-1}]	2.457×10^{-6}
Fuel molar fraction (equal to a pre-reforming rate of 30%)	0.17 CH_4, 0.48 H_2O 0.26 H_2, 0.02 CO, 0.04 CO_2
Fuel steam/carbon ratio	2.85
Fuel/air flow time constant [s]	2/–
Air inlet flow [mol s^{-1}]	8.282×10^{-5}
Air molar fraction	0.21 O_2, 0.79 N_2
Average cell voltage [V]	0.7 (cascaded cell: 7 V)
Fuel utilization [%]	85%

flow direction as a consequence of low temperatures and high polarization at the fuel inlet of the cell. Even if the temperature increases up to a cell length of 7 cm, the local current density decreases from a cell length of 4 cm. This is because the decreasing of the Nernst voltage and the increasing of concentration-sensitive losses are larger than the influence of temperature-sensitive losses. At a cell length of 7 cm the temperature reaches a maximum of 1268 K. The temperature drop in the last third of the cell length occurs due to radiative and convective heat transfer between air preheater tube and cathode.

The local cell voltage shows a slightly maximum in the middle of the cell length, which can be explained by ohmic losses in the anode and cathode. This is because the current collectors (Fig. 1) leads the highest current density at the beginning of the anode (cell length: 0 cm) and at the end of cathode (cell length:10 cm). The average ohmic resistances

$$R_{\mathrm{An(Ca)}} = \frac{\delta R_\delta}{\Delta A_i} \tag{39}$$

of each electrode and each cell slice are adjusted to 4.23×10^{-4} Ω to reach the same average power density as the cascaded micro-tubular cell. This is much lower than the average ohmic resistance of the cascaded concept. On these conditions

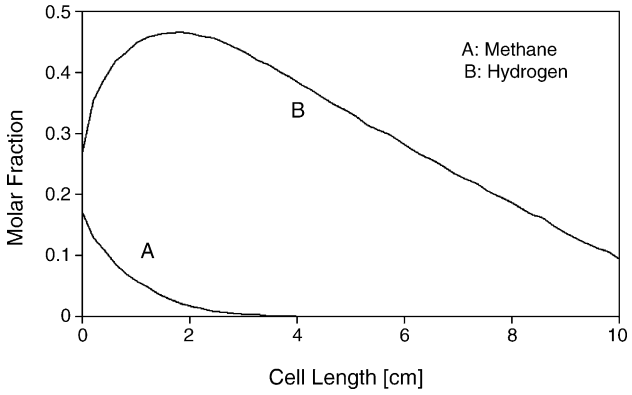

Fig. 9. Hydrogen and methane fraction of the cascaded cell.

the common micro-tubular cell reaches a voltage of 0.7 V at an all over current of 2.3 A which is equal to an average current density of 244 mA cm^{-2} and an average power density of 170 mW cm^{-2}.

In this study, the cascaded micro-tubular cell should operate on the same effective area, average cell voltage, gas inlet flow rates and fuel utilization as the common micro-tubular cell. To fulfil these conditions with 10 cascades, the all over cell voltage must be 10 times higher and the current must be 10 times lower than the values of the common cell. Because the all over current of each cascade must be the same, the current density is distributed over the whole cell length. This explains why the maximum of hydrogen fraction is displaced to the cell inlet (Fig. 9) and why the decrease of the hydrogen fraction shows a linear characteristic.

The average current density (Fig. 10) related to the cascade cell area has the same value as the average current density of the common cell. The cascade voltage increases along the flow direction as a consequence of low temperatures and high polarization at the fuel inlet of the cell. From a cell length of 4 cm the cascade voltage decreases due to the decreasing Nernst voltage and the increasing of polarization losses.

The temperature profile of the cascaded micro-tubular cell shows the similar tendency with the common micro-tubular cell. The temperature maximum of 1266 K is located at 7 cm of cell length. On these conditions the cascaded micro-tubular cell reaches a voltage of 7 V at an all over current of 0.23 A

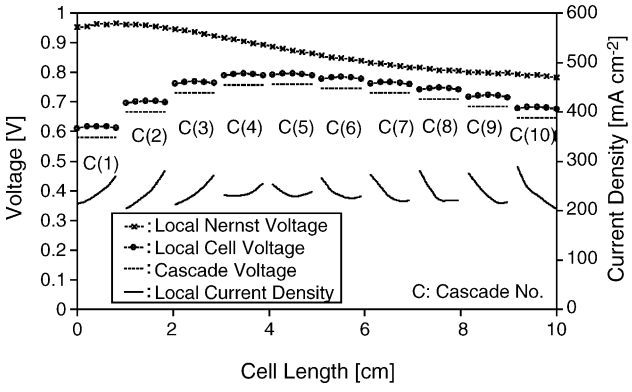

Fig. 10. Local voltage and current density of the cascaded cell.

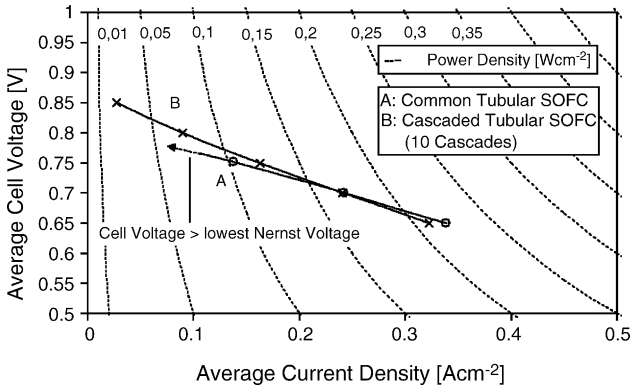

Fig. 11. *U*/*I*-characteristics of the common and cascaded cell.

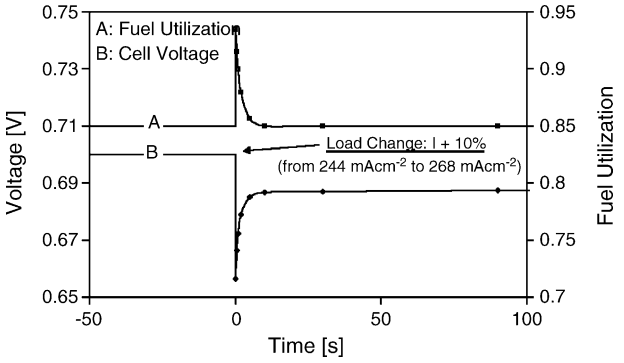

Fig. 12. Load change of the common cell.

which is equal to an average current density of 244 mA cm^{-2} per cascade and an average power density of 170 mW cm^{-2} per cascade.

Fig. 11 shows the average *U*/*I*-characteristic of the common and cascaded micro-tubular cell. As mentioned before the ohmic resistance (anode and cathode) of the common cell is adjusted much lower than the ohmic resistance of the cascaded cell. Hence, the average cell voltage (0.7 V) of both cells is the same at an average current density of 244 mA cm^{-2}. At lower current densities than 100 mA cm^{-2} the voltage of the common cell is limited by the Nernst voltage at the fuel outlet. To guarantee the operation of the common cell in this performance range the fuel utilization has to be decreased which involves a lower efficiency.

As shown in Fig. 11, the cascaded concept gives the opportunity to operate at lower part load conditions than the common concept without decreasing the fuel utilization. At current densities higher than 100 mA cm^{-2} both cells show similar performance for the ohmic and electrochemical assumptions of this study.

3.2. Transient behavior

In common energy supply applications electrical current and voltage are controlled to react on changes in load demand. In fuel cell applications inverter are used to fulfil these requirements. To decouple the transient behavior of the SOFC from that of the inverter, the load change is simulated for an increased current of +10%. The transient electrical response and the change in temperature profile are simulated. The inlet gas compositions and inlet temperatures of fuel and oxidant are kept constant in this simulation. In practical SOFC systems fuel flow rates are controlled to keep the steady state fuel utilization ratio constant. This implies that reacting species are delivered with a time delay (Eq. (38)). In this study, the air ratio is kept constant. It is assumed that the time constant of the fuel cell capacities were negligible in comparison to the time constant of the gas deliveries. The perfusion of the gas streams through the cell occurs in a time lower than 0.1 s. Therefore, the transient behavior of gas distributions along the cell length was neglected as well.

As shown in Fig. 12, the fuel utilization of the common micro-tubular cell increases up to 94% at a time of 0 s. The minimum cell voltage during this load change is 0.656 V. The polarization losses at the time of 0 s are much higher compared to the losses at the new steady state condition because of the temporary high fuel utilization. This is because the cell voltage increases with the decreasing fuel utilization. At the new steady state condition the fuel utilization is controlled to 85%. The voltage reaches a final value of 0.687 V. The fuel utilization could have a limiting influence in load change, if the reacting species are delivered with high time delays. This effect applies especially to the common micro-tubular cell, which is from a theoretical point of view unable to reach cell voltages above the lowest Nernst voltage.

Fig. 13 shows the transient temperature profiles of the common micro-tubular cell. At a time of 300 s the temperature profile reaches 90% of the final profile ($\tau = \infty$). The temperature maximum increases from 1268 K up to 1288 K. Due to a local displacement in current density the temperature maximum is displaced slightly to the cell inlet.

As shown in Fig. 12, the influence of changing in cell temperature on polarization losses can be neglected. The outlet temperature of gas species increases from 1131 to 1142 K at the cathode and from 1173 to 1188 K at the anode. In deviation to this study the air ratio would be controlled in practical SOFC stacks to keep the maximum temperature of the cell constant.

The transient response of the cascaded micro-tubular cell shows a similar behavior with the common micro-tubular cell. Even if the temporary high fuel utilization occurs during this load change as well, the minimum average cell voltage (0.67 V) is higher than the voltage of the common micro-tubular cell (0.656 V). This can be explained by the fact that the change in

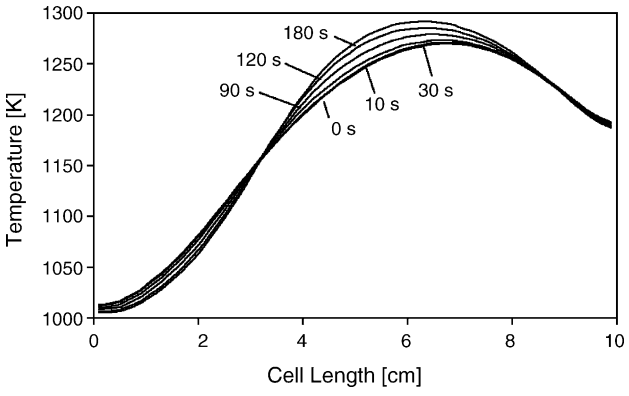

Fig. 13. Temperature profile of the common cell.

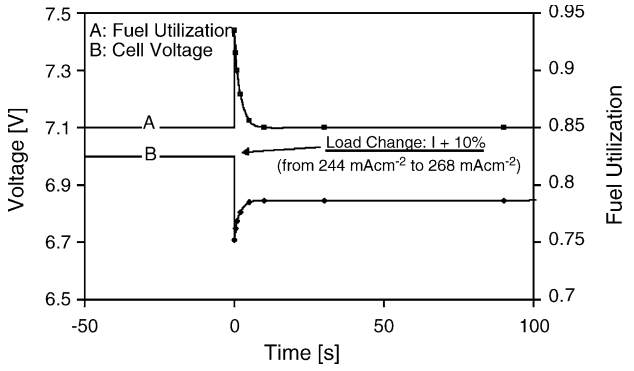

Fig. 14. Load change of the cascaded cell.

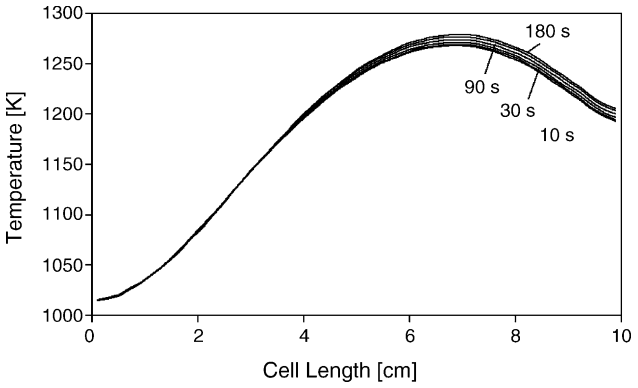

Fig. 15. Temperature profile of the cascaded cell.

polarization is mainly located in the last half of the cascaded cell. At the new steady state condition the fuel utilization is controlled to 85%. The voltage reaches a final value of 6.85 V (Fig. 14).

The transient temperature profiles of the cascaded micro-tubular cell are shown in Fig. 15. At a time of 300 s the temperature profile reaches 95% of the final profile ($\tau = \infty$). The temperature maximum increases from 1266 K up to 1282 K. Due to the regular distribution in current density the temperature profile shows no displaced at new steady state condition. The outlet temperature of gas species increases from 1149 to 1160 K at the cathode and from 1196 to 1210 K at the anode.

In comparison to the transient response of the common micro-tubular cell the cascaded concept shows a more favorable behavior with respect to voltage drop and temperature distribution.

4. Conclusion

A two-dimensional model was developed to simulate the steady state and transient characteristics of tubular SOFC. Steady state and transient characteristics of a common and cascaded micro-tubular cell with a cell diameter of 2 mm were simulated and compared.

In this study, the cascaded micro-tubular cell has the same effective area, average cell voltage, gas inlet flow rates and fuel utilization as the common micro-tubular cell. With 10 cascades the all over cell voltage must be 10 times higher and the current must be 10 times lower than the values of the common cell. To reach a common average power density at an average voltage of 0.7 V the average ohmic resistance (anode/cathode) of the common micro-tubular cell were adjusted to $4.23 \times 10^{-4}\ \Omega$. This is 84 times lower than the average ohmic resistance of the cascaded concept. This resistance depends strongly on the thickness of anode and cathode, wire thickness and contact resistances. Even if all over current is reduced by the factor of cascades and power losses depends on all over current approximately to square, the current density in z-direction could reach very high values, with a small thickness of the anode or cathode. Compared to the ohmic resistance of the tubular cell developed by Westinghouse the adjusted ohmic resistance of the common micro-tubular cell is this still a low value. However, future development in cell concepts may reach the adjusted resistance of the common micro-tubular cell of this study. In that case, the common micro-tubular cell could reach the same power density as the cascaded micro-tubular cell of this study.

The U/I-characteristic of the cascaded cell shows that higher average voltages can be reached at low average current densities compared to the common micro-tubular concept.

The transient electrical response and the change in temperature profile were simulated. The inlet gas compositions and inlet temperatures of gas species were kept constant. The fuel flow rates were controlled to keep the steady state fuel utilization ratio constant. The results of the transient simulation show the quick response to a load change in the common micro-tubular cell and cascaded concept as well. During this load change, the minimum average cell voltages reached values of 0.67 V for the cascaded cell concept and 0.656 V for the common cell concept. It is supposed that the cascaded cell concept could work on higher load changes than the common cell concept.

Future work should involve the evaluation of the simulation results with experimental data. It is assumed that the cascaded cell concept offers a high potential in optimization with respect to the number of cascades, the anode and cathode thickness respectively. Not at least economic analysis including the peripheral system costs should be taken into account.

References

[1] K. Kendall, M. Palin, A small solid oxide fuel cell demonstrator for microelectronic applications, J. Power Sources 71, Seite 268–270, 1998.
[2] W. Winkler, Brennstoffzellenanlagen, Springer-Verlag, 2003.
[3] P. Nehter, Thermodynamische und ökonomische Analyse von Kraftwerksprozessen mit Hochtemperatur-Brennstoffzelle SOFC, Shaker-Verlag, 2005.
[4] D.J. Hall, R.G. Colclaser, Transient Modeling and Simulation of a Tubular Solid Oxide Fuel Cell, IEEE Trans. Energy Conver. 14 (3) (1999).
[5] M. Mogensen, T. Lindegaard, Riso National Laboratory, Proceedings of the Third International Symposium on Solid Oxide Fuel Cells, The Electrochemical Society, 1993, p. 484.
[6] P.D. Neufield, A.R. Janzen, R.A. Aziz, J. Chem. Phys. 57 (1972) 1100.
[7] S.H. Chan, K.A. Khor, Z.T. Xia, A complete polarization model of a solid oxide fuel cell and its sensitivity to the change of cell component thickness, J. Power Sources 93 (2001) 130–140.
[8] E. Achenbach, Ch. Rechenauer, F.Z. Jülich, R.W.T.H. Aachen, Dreidimensionale mathematische Modellierung des stationären und

instationären Verhaltens oxidkeramischer Hochtemperatur-Brennstoffzellen, 1993.
[9] I. Drescher, F.Z. Jülich, R.W.T.H. Aachen, Kinetik der Methan-Dampf-Reformierung, Dissertation, 1999.
[10] J. Metzger, A.G. Siemens, Untersuchung der Stoffumsätze an mit Methan betriebenen Festelektrolyt-Brennstoffzellen, 1998.
[11] T. Takeguchi, Y. Kani, T. Yano, R. Kikuchi, K. Eguchi, K. Tsujimoto, Y. Uchida, A. Ueno, K. Omoshiki, M. Aizawa, Study on reforming of CH_4 and C_2 hydrocarbons and carbon deposition on Ni–YSZ cermets, J. Power Sources 112 (2002) 588–598.
[12] A.L. Dicks, K.D. Pointon, A. Swann, The Kinetics of the methane steam reforming reaction on a nickel/zirconia anode, in: Proceedings of the Third European SOFC Forum, Nantes, June 1998, 1998, pp. 249–265.
[13] A. Selimovic, Lund University (Sweden), Modelling of Solid Oxide Fuel Cells, Applied Analysis of Integrated Systems with Gas Turbines, Dissertation, 2002.
[14] W.L. Lundberg, R.A. Holmes, J.E. King, G.A. Israelson, P.R. Zafred, R.E. Kothmann, M.D. Moeckel, S.E. Veyo, Siemens–Westinghouse: A High Efficiency PSOFC/ATS-Gas Turbine Power System, Final Report, 2001.